Differential Power Processing Converter Enhancing Energy Yield of Curved Solar Roofs of Plug-in Hybrid Electric Vehicles

Masatoshi Uno, *Member*, *IEEE*, Hayato Sato, Tetsuaki Ishikawa

Abstract—In photovoltaic (PV) panels consisting of multiple substrings connected in series, mismatch in substring characteristics due to partial shading causes the significant reduction in energy yield and the occurrence of multiple maximum power points. In solar roofs of plug-in hybrid electric vehicles (PHEVs), substring characteristics are always unavoidably mismatched due to the curvature of solar roofs, resulting in the mismatch issues similar to partial shading. Various kinds of differential power processing (DPP) converters have been proposed to preclude mismatch issues in traditional flat PV panels. The key contributions and novelties of this paper are summarized as follows. Firstly, uneven irradiance on the solar roof of Prius PHEVs is investigated. Secondly, existing DPP converter architectures are reviewed to select a proper DPP converter topology for PHEV applications. Thirdly, the selected topology is improved to be better suitable for PHEV applications, followed by the detailed operation analysis. Lastly, the experimental results of the laboratory and field testing using a prototype are presented. Field testing using an actual solar roof of Prius PHEV was performed, and the results demonstrated the daily energy yield enhancement of 4%–5% by the proposed DPP converter.

Keywords—*Differential power processing (DPP) converter, LLC converter, partial shading, plug-in electric vehicle (PHEV), solar roof.*

I. INTRODUCTION

Photovoltaic (PV) power generation systems have become a global trend to reduce carbon emission and reliance on fossil fuels. To increase and maximize the energy yield form PV systems, vigorous research and development efforts are currently underway in industrial and academic sectors. Power electronics is one of the important key realms to realize more efficient PV systems. In the power electronics field, efficient power converters have already been developed and commercialized by various manufacturers. However, efficient converters alone cannot maximize the energy yield of PV systems because characteristic mismatch in series-connected PV panels or substrings significantly impairs PV panel utilization factors and reduces the energy yield of PV systems.

In general, PV panels are subdivided into substrings—ordinary PV panels consist of three substrings connected in series, each with a parallel-connected bypass diode. Substring characteristics are mismatched if a PV panel is partially shaded. The shaded substring is less capable of generating current, and therefore a panel current detours through a parallel-connected bypass diode, as shown in Fig. 1(a). The shaded substring no longer generates current as its voltage is subzero value due to a forward voltage drop of the bypass diode, though it can potentially generate power to some extent. Partial shading equivalent to 10% area of a PV panel reportedly leads to 20%–30% decrease in an annual energy yield on a residential rooftop [1]. In addition, due to the characteristic mismatch, multiple maximum power points (MPPs), including one global and some local MPPs, appear on a *P–V* characteristic, as shown in Fig. 1(b), that might hinder and confuse ordinary MPP tracking algorithms.
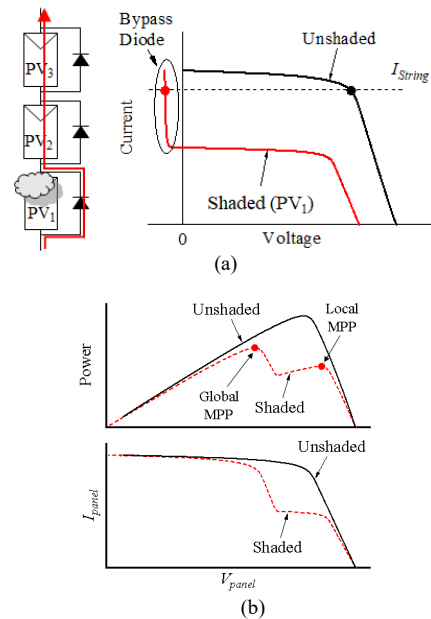

Fig. 1. (a) Mismatched substring characteristics due to partial shading. (b) Panels characteristics with/without partial shading.

M. Uno and H. Sato are with the College of Engineering, Ibaraki University, Hitachi 316-8511, Japan (e-mail: masatoshi.uno.ee@vc.ibaraki.ac.jp).
T. Ishikawa is with Kojima Industries Corporation, Aichi, Japan (e-mail: tetsuaki-ishikawa@kojima-tns.co.jp).

To cope with such partial shading issues, a variety of differential power processing (DPP) converters, or voltage equalizers, have been proposed and developed [2]–[32]. DPP converter architectures can be roughly divided into three groups, depending on power redistribution scenarios, as listed in Fig. 2: the adjacent PV-to-PV, PV-to-isolated port (IP), and panel-to-PV redistribution architectures. Fig. 2 illustrate the notional architectures for three substrings.

In the adjacent PV-to-PV architecture [see Fig. 2(a)], nonisolated bidirectional converters, such as PWM converters [3]–[11], switched capacitor converters [12]–[19], are usually employed as DPP converters. Adjacent substrings exchange power through DPP converters to virtually unify substring characteristics or to achieve individual MPPT operations [6]–[8]. The power transfer path is limited only between neighboring substrings, and therefore, power conversion losses tend to collectively soar as the number of substrings and DPP converters increases.

The PV-to-IP architecture [see Fig. 2(b)] overcomes the issue of collective power conversion loss as it allows direct power transfer among remoted substrings via the IP. Isolated bidirectional flyback converters are generally employed as DPP converters in this architecture [20]–[26]. However, the requirement of multiple bidirectional flyback converters, each containing two switches and a flyback transformer, is an obvious drawback from the viewpoints of the cost and volume.

The panel-to-PV architecture [Fig. 2(c)] also allows the direct power transfer from a panel to substring(s). DPP converters in this architecture are essentially a single-input–multi-output converter [27]–[32], and hence, the number of DPP converters in this system can only one regardless of the number of substrings. In addition, the total switch count can also be significantly reduced to a few, realizing the simplified circuit.
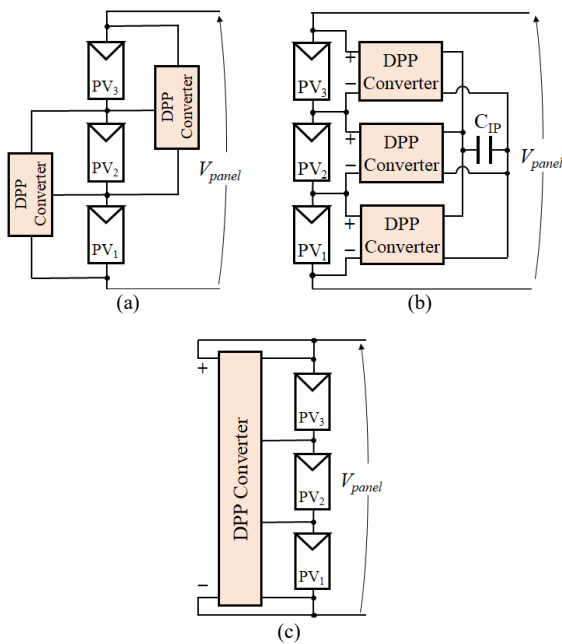
Regardless of types of DPP converter architectures or topologies, a fraction of generated power of unshaded substrings is transferred to shaded ones so that all substrings operate at the same voltage or even at each MPP. In other words, DPP converters virtually unify substring characteristics under partial shading conditions. DPP converters reportedly improve the energy yield by a few tens of percent, depending on shading patterns.

At the same time, applications of PV power generation are rapidly expanding from traditional stationary systems, such as residential rooftop PV systems, solar power plants, etc., to vehicular applications. Prius plug-in hybrid electric vehicles (PHEVs), for example, are equipped with a so-called solar roof that is optionally used to support low-voltage rechargeable batteries. The solar roof contains 56 cells that are subdivided into seven substrings. Contrary to traditional standard flat PV panels, the solar roof is mounted on a curved surface, as shown in Fig. 3(a). The irradiance on the solar roof is naturally uneven due to the curved surface, as illustrated in Fig. 3(b), resulting in mismatched substring characteristics. Since an area of PHEV rooftops is very limited and precious, the power generation of the solar roof is desirably maximized with precluding the negative influences of the characteristic mismatch originating from the uneven irradiance.

The decreased energy yield of solar roofs due to the uneven irradiance would be precluded by DPP converters, similar to partial shading cases. However, to our best knowledge, conventional DPP converters in the past works have been chiefly developed for standard 60- or 72-cell panels comprising three substrings, and DPP converters for PHEV 56-cell solar roofs comprising seven substrings have been neither reported nor investigated.

This paper presents a DPP converter for solar roofs of Prius PHEVs and investigates the energy yield of actual solar roofs. The key contributions and novelties of this paper are summarized as follows.

- Uneven irradiance on the solar roof of Prius PHEVs is investigated
- Existing DPP converter architectures are reviewed to select a proper DPP converter topology for PHEV applications
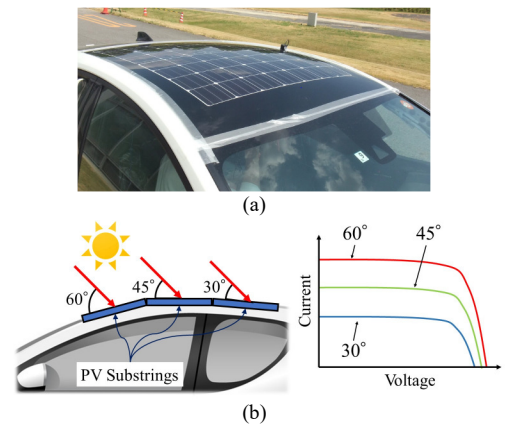

Fig. 2. DPP architectures. (a) Adjacent PV-to-PV, (b) PV-to-IP, and (c) panel-to-PV DPP architectures.

Fig. 3. (a) Solar roof of Prius PHEV. (b) Image of uneven irradiance due to curved surface.

- The selected topology is improved to be better suitable for PHEV applications, followed by the detailed operation analysis
- Experimental verification tests based on the field testing using an actual solar roof of Prius PHEV

The rest of this paper is organized as follows. Section II investigates the irradiance mismatch on a solar roof due to the curvature in order to model mismatched substring characteristics. In Section III, DPP converters and architectures are reviewed, and a suitable DPP converter architecture and topology will be selected with considering the solar roof structure and requirements in PHEVs. The selected DPP converter topology is improved to be better suitable for PHEVs in Section IV. The detailed operation analysis will be performed in Section V, followed by simulation analyses using the derived substring models and dc equivalent circuit in Section VI. Section VII presents the experimental results of laboratory tests using solar array simulators and field testing using an actual solar roof of Prius PHEV.

II. SOLAR ROOF OF PRIUS PHEV

This section investigates the irradiance mismatch on solar roofs of Prius PHEVs. Mismatched irradiance and substring characteristics are modeled with considering sun angles and the curved surface of solar roofs.

A. Specifications of Solar Roof of Prius PHEV

A solar roof of Prius PHEVs consists of seven substrings, each comprising eight cells connected in series. Each cell is a monocrystalline silicon PV cell with 12.5×12.5 cm (156 cm^2), and its short-circuit current and an open-circuit voltage are 5.95 A and 0.745 V, respectively. The rated maximum power of a solar roof is 180 W.

The configuration and curvature of the solar roof are depicted in Fig. 4(a). Positions of cells in the solar roof can be designated by row A–G and column a–h. The cell at i-th row and j-th column is expressed as Cell$_{i,j}$. The row and column
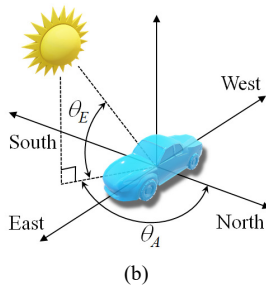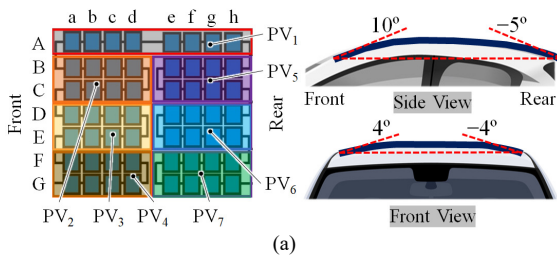

(a)

(b)

Fig. 4. (a) Configuration and curvature of solar roof. (b) Irradiance condition of solar roofs.

TABLE I
ROW ANGLES OF SOLAR ROOF

	A	B	C	D	E	F	G
Angle [°]	4	3	1	0	-1	-3	-4

TABLE II
COLUMN ANGLES OF SOLAR ROOF

	a	b	c	d	e	f	g	h
Angle [°]	10	6	2	0	-1	-3	-4	-5

angles in Prius PHEVs are shown in Tables I and II, respectively. The curvature of the solar roof viewed from the front is symmetric. The side-view angles, on the other hand, are asymmetric, and its angles vary between −5º and 10º, as shown in Table II.

B. Irradiance Conditions of Solar Roofs

Irradiance conditions on solar roofs vary depending on seasons and time. The varying irradiance conditions are characterized by two sun angles of the azimuth θ_A and elevation θ_E, as illustrated in Fig. 4(b). In this study, we consider the cases that a PHEV facing east in an open-air parking lot in Miyoshi City, Japan (east longitude of 137º and northern latitude of 35º). The degree of irradiance mismatch on solar roofs is determined by not only θ_A and θ_E but also row and column angles of solar roofs.

Around noon, all substrings receive relatively uniform irradiance because of $\theta_A \approx 180º$ and high θ_E, and therefore, substring characteristics tend to be uniform. In the morning and afternoon, on the other hand, irradiance with shallow θ_E results in uneven irradiance due to the curved surface. In addition, the longitudinal curvature of the solar roof is asymmetric, as shown in Fig. 4(a) and Table II, and therefore, substring characteristics in the morning and afternoon are mismatched to a different extent. Two cases at 9:00 ($\theta_A = 135º$ and $\theta_E = 30º$) and 15:00 ($\theta_A = 235º$ and $\theta_E = 22º$) on October are investigated in this paper.

C. Irradiance Variation on Solar Roof

Estimated irradiance levels of cells on the solar roof at 9:00 were calculated with considering row and column angles, as shown in Table III. Sunlight comes from the front right side of the vehicle, and therefore, cells on the front right side receive relatively high irradiance. The highest and lowest irradiance levels are 424 W/m^2 at Cell$_{A.a}$ and 277 W/m^2 at Cell$_{G.h}$. Hence, the maximum irradiance difference at 9:00 is 147 W/m^2.

Irradiance levels at 15:00 are shown in Table IV. Irradiance levels of cells on the rear right side are relatively high in the afternoon. The highest irradiance level of 389 W/m^2 can be found at Cell$_{A.h}$, whereas the lowest irradiance of 200 W/m^2 occurs at the diagonal position of Cell$_{G.a}$. The maximum irradiance difference is 189 W/m^2, and the degree of irradiance mismatch at 15:00 is severer than that at 9:00 due to the asymmetric curvature of the solar roof viewed from the side [see Fig. 4(a)].

D. Substring Characteristics of Solar Roof

Substring characteristics are modeled based on a single-

TABLE III
IRRADIANCE OF CELLS AT 9:00 ($\theta_A = 135°$ AND $\theta_E = 30°$)

	a	b	c	d	e	f	g	h
A	424	402	385	372	359	349	340	331
B	415	393	375	363	350	340	331	322
C	405	383	366	353	341	330	322	313
D	397	375	357	345	331	322	313	305
E	388	365	348	335	327	313	304	296
F	378	356	338	326	313	303	294	286
G	368	345	328	315	303	293	285	277

TABLE IV
IRRADIANCE OF CELLS AT 15:00 ($\theta_A = 235°$ AND $\theta_E = 22°$)

	a	b	c	d	e	f	g	h
A	255	292	319	337	355	368	379	389
B	246	283	309	328	346	359	370	380
C	237	274	300	319	331	350	361	372
D	228	265	292	310	328	341	353	363
E	220	256	283	301	318	332	344	354
F	210	247	273	292	310	323	334	345
G	200	237	263	282	300	313	325	335

TABLE V
KEY PARAMETERS OF SUBSTRINGS AT 9:00 ($\theta_A = 135°$ AND $\theta_E = 30°$)

	PV_1	PV_2	PV_3	PV_4	PV_5	PV_6	PV_7
I_{sc} [A]	1.89	2.02	1.92	1.80	1.79	1.69	1.59
V_{oc} [V]	4.71	4.75	4.72	4.68	4.68	4.65	4.62
I_{mp} [A]	1.80	1.92	1.82	1.71	1.70	1.61	1.51
V_{mp} [V]	3.77	3.80	3.78	3.74	3.74	3.72	3.70

TABLE VI
KEY PARAMETERS OF SUBSTRINGS AT 15:00 ($\theta_A = 235°$ AND $\theta_E = 22°$)

	PV_1	PV_2	PV_3	PV_4	PV_5	PV_6	PV_7
I_{sc} [A]	1.46	1.35	1.26	1.14	1.89	1.82	1.71
V_{oc} [V]	4.58	4.55	4.52	4.49	4.71	4.69	4.66
I_{mp} [A]	1.39	1.28	1.20	1.08	1.80	1.73	1.62
V_{mp} [V]	3.66	3.64	3.62	3.59	3.77	3.75	3.73

Fig. 5. Modeled individual substring characteristics at (a) 9:00 and (b) 15:00.

diode model and can be characterized by four parameters of short-circuit current (I_{sc}), open-circuit voltage (V_{oc}), and current and voltage at an MPP (I_{mp} and V_{mp}). The four key parameters are determined based on the estimated irradiance of cells shown in Tables III and IV.

The key parameters and substring characteristics at 9:00 are shown in Table V and Fig. 5(a), respectively. All substring characteristics differ depending on positions and irradiance levels of cells. The values of I_{sc} are dependent on a cell receiving the lowest irradiance in each substring. I_{sc} of PV_1, for example, is determined by $Cell_{A.h}$ that receives the lowest irradiance (331 W/m²) in PV_1. Although the highest irradiance on the panel as a whole occurs at $Cell_{A.a}$ in PV_1, I_{sc} of PV_1 is inferior to that of PV_2 because the lowest irradiance in PV_2 (i.e., 353 W/m² at $Cell_{C.d}$) is higher than that in PV_1 (331 W/m² at $Cell_{A.h}$).

The determined key parameters and individual substring characteristics at 15:00 are shown in Table VI and Fig. 5(b), respectively. Contrary to the case at 9:00, substrings near the rear right side exhibit larger I_{sc} than those near the left front side. The characteristic mismatch is more accentuated due to the severer irradiance mismatch.

III. DPP CONVERTER TOPOLOGY SELECTION FOR PHEVs

A. Differences between Solar Roofs and Standard Flat PV panels

A proper DPP converter topology should be selected with considering specifications of solar roofs and requirements in PHEVs. Hence, this subsection describes major differences between solar roofs and traditional flat PV panels before discussing the topology selection.

From the viewpoint of the topology selection, the most critical difference is the number of substrings. As depicted in Fig. 4(a), solar roofs of Prius PHEV consist of seven substrings, each comprising eight cells connected in series. Standard 72-

cell PV panels, on the other hand, comprise three substrings, each having 24 cells. The increased substring number poses a significant impact on the topology selection and circuit design.

In Prius PHEVs, a junction box containing seven bypass diodes is installed behind the ceiling with an allowed space of a few centimeters. Given that the junction box containing bypass diodes is replaced with a DPP converter, bulky circuit elements should desirably be eliminated, and low-profile components should be used.

The reliability is also the primary importance, similar to conventional PV panels. To assure the high reliability, the number of circuit elements is desirably be reduced. To this end, the switch count should be minimized—the switch count is an

index of the circuit complexity as each switch requires a gate driver and its auxiliary power supply. Furthermore, DPP converters should preferably be able to operate without feedback control nor voltage and current sensors for substrings.

B. Architecture Selection

As mentioned in Section I, DPP converter architectures can be categorized into three groups, as shown in Fig. 2. This subsection discusses the pros and cons of these three architectures to select the best suitable DPP converter architecture for the PHEV applications.

In the adjacent PV-to-PV architecture [Fig. 2(a)], each DPP converter is simple and compact. However, since the power transfer is limited between adjacent substrings, power conversion losses tend to collectively soar in solar roofs consisting of seven substrings. For example, power from a substring at one end must traverse six DPP converters before reaching a substring at the other end. Another concern is that six DPP converters, each containing switches, are indispensable, resulting in the increased system and circuit complexities.

The PV-to-IP architecture [see Fig. 2(b)] would achieve the higher energy yield by overcoming the issue of the collective power conversion losses. However, this architecture requires seven DPP converters, each containing a flyback transformer and two switches, increasing the system complexity, cost, and volume. The increased volume due to the requirement of multiple transformers is not preferable in PHEV applications as an allowed space for DPP converters is very limited.

Meanwhile, with the panel-to-PV architecture [Fig. 2(c)], the number of DPP converters can be only one even for seven substrings in solar roofs. Furthermore, some of the conventional DPP converters of the panel-to-PV architecture realize single magnetic topology (as will be discussed in the next subsection), achieving the reduced circuit volume. Thus, the panel-to-PV DPP architecture would be a preferable solution from the viewpoint of the complexity and reliability in PHEV applications. In the following subsection, a proper DPP converter topology of the panel-to-PV architecture will be selected with considering various aspects.

C. DPP Converter Topology Selection

Three DPP converter topologies of the panel-to-PV architecture have been proposed, as listed in Fig. 6. These three topologies are compared from the viewpoint of the design difficulty, the necessity of feedback control, and circuit volume.

The multi-winding flyback converter [Fig. 6(a)] is the simplest and most straightforward topology as a single-input–multi-output converter [27]. However, the design hurdle of the multi-winding transformer is cited as a top concern because parameters of the multiple secondary windings (e.g., turn ratios and leakage inductances) need to be strictly matched to achieve adequate performance [33]. In addition, the multi-winding flyback transformer tends to be even bulkier than ordinary transformers because of the existence of multiple secondary windings, and therefore, this topology might not fit the allowed space in PHEVs.

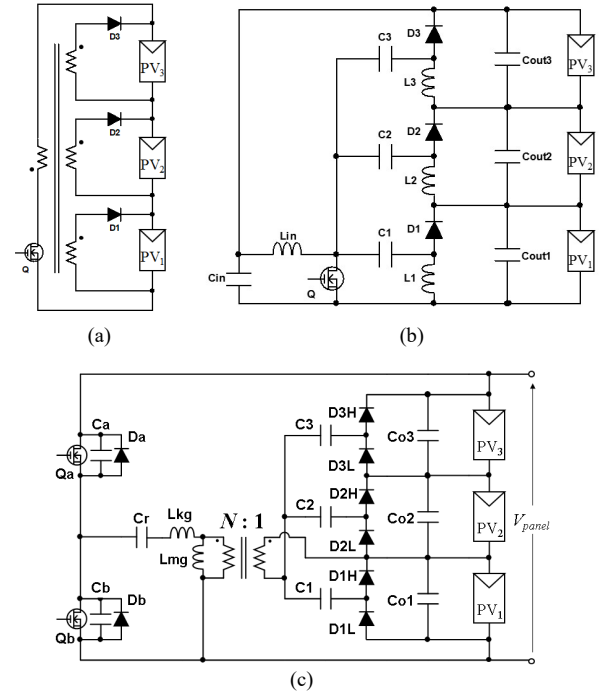The DPP converter based on the multi-stacked buck-boost

Fig. 6. DPP converters for panel-to-PV architecture. (a) Multi-winding flyback converter, (b) multi-stacked buck-boost converters, (c) LLC resonant voltage multiplier.

converters [Fig. 6(b)] realizes the lack of transformerless topology at the cost of multiple inductors [28], [29]. However, this topology must operate with an extreme duty cycle of $d = 0.125$ for the seven-substring configuration because its panel-to-substring voltage conversion ratio is $d/(1 - d)$. Furthermore, this DPP converter must be properly controlled, otherwise it unnecessarily redistributes power from a panel to substrings, causing unnecessary power conversion losses.

The LLC (inductor-inductor-capacitor) resonant voltage multiplier [Fig. 6(c)] requires neither a multi-winding transformer nor feedback control [30]–[32]. Driving switches with a fixed 50% duty cycle at a fixed switching frequency achieves automatic voltage equalization [30], allowing the simplified circuit and design. Thus, this DPP converter topology meets the requirements of solar roofs of PHEVs. However, the transformer miniaturization is desirable so that this DPP converter can be installed in the limited gap of ceilings in PHEVs. The next section proposes an improved version of the LLC resonant voltage multiplier to reduce the transformer volume.

IV. LLC RESONANT VOLTAGE MULTIPLIER WITH INTERLEAVED VOLTAGE DIVIDER

A. Circuit Description

The improved version of the LLC resonant voltage multiplier is shown in Fig. 7. The circuit on the transformer secondary side (i.e., the voltage multiplier) is identical to that of the conventional one. Meanwhile, an interleaved voltage divider is employed on the primary side to halve the applied voltage to the LLC resonant tank and to double the effective switching
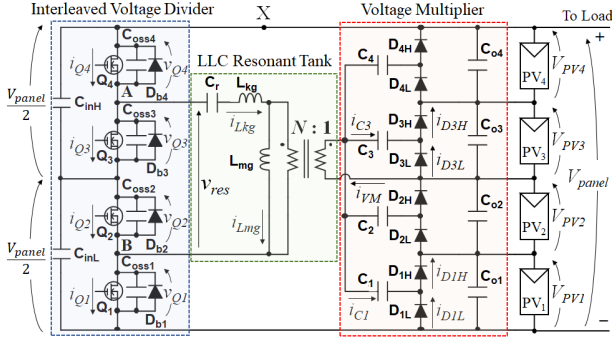
Fig. 7. Improved DPP converter based on LLC resonant voltage multiplier with interleaved voltage divider

frequency.

Switches Q_1 and Q_2 operate in a complementary mode, and so do Q_3 and Q_4. Inner switches of Q_2 and Q_3 are driven with a fixed 75% duty cycle at a fixed switching frequency in 180º out of phase. Similar to traditional LLC resonant converters, all the switches are turned on and off with zero voltage switching (ZVS) manners. Voltages of the input smoothing capacitors, C_{inH} and C_{inL}, are automatically balanced to be $V_{panel}/2$.

B. Control Scheme

Similar to the conventional LLC resonant voltage multiplier, the proposed DPP converter operates with open-loop control. Operating the DPP converter with a fixed duty cycle at a fixed switching frequency achieves an automatic voltage equalization for all substrings—the proposed DPP converter automatically feeds currents for weak substrings, as discussed with the dc equivalent circuit in Section V-B. In other words, neither a feedback control loop nor voltage/current sensors are necessary to preclude the characteristic mismatch issues.

C. Major Features

Similar to the conventional LLC resonant voltage multiplier [see Fig. 6(c)], the proposed DPP converter operates with a fixed duty cycle at a fixed switching frequency without feedback control. Even with open-loop control, the proposed DPP converter automatically equalizes substring voltages, allowing the simplified circuit and design by eliminating a feedback control loop.

Thanks to the halved applied voltage and doubled effective switching frequency, the volt-sec product of the transformer winding is one-fourth that of the conventional LLC resonant voltage multiplier. According to the area product method [34], the transformer volume can be reduced, and therefore, this topology is suitable for solar roofs in PHEVs where DPP converters are supposed to be installed in a limited space.

Poor design flexibility is cited as a major drawback of the proposed DPP converter. For example, voltages applied to switches, input smoothing capacitors (C_{inH} and C_{inL}), and the resonant tank are as high as half the panel voltage (i.e., $V_{panel}/2$). Therefore, when the number of substrings in the panel changes, these components need to be reselected. However, as long as the number of substrings in the panel is fixed, the poor design flexibility of the proposed DPP converter would not be an issue.

V. OPERATION ANALYSIS

A. Operation Modes

Although solar roofs consist of seven substrings, this subsection deals with the DPP converter for four substrings connected in series for the sake of simplicity. Current flow paths in the voltage multiplier vary depending on mismatched conditions. A mismatched condition where substrings of PV_1 and PV_3 are weaker than others is explained as a representative case. The operation analysis is performed on the premise that all circuit elements are ideal, and the magnetizing inductance L_{mg} is far larger than the leakage inductance L_{kg} (i.e., $L_{mg} >> L_{kg}$).

Theoretical key operation waveforms and current flow paths are shown in Figs. 8 and 9, respectively. v_{GS1}–v_{GS4} are the gating signals for switches Q_1–Q_4. Q_2 and Q_3 are driven 180º out of phase with a 75% duty cycle at a fixed switching frequency for the interleaving operation. Operation modes are divided into eight modes, but first four modes (Modes 1–4) are symmetric to the last four modes. Hence, only the first four modes are explained to save page length.

Mode 1 [Fig. 9(a)]: Before this mode (i.e., in Mode 8), the body diode of Q_4 is conducting. At the beginning of Mode 1, v_{GS4} is applied to turn on Q_4, achieving ZVS turn-on. Q_2 and Q_4 are conducting, and the LLC resonant tank is connected to C_{inH}. The voltage applied to the resonant tank, v_{res}, is equal to $V_{panel}/2$. The current of magnetizing inductance i_{Lmg} linearly increases while the leakage inductance current i_{Lkg} sinusoidally changes. On the transformer secondary side, currents flow through the high-side diodes of D_{1H} and D_{3H} that are connected in parallel with weak substrings of PV_1 and PV_3. This mode lasts until i_{Lkg} becomes equal to i_{Lmg}.

Mode 2 [Fig. 9(b)]: Q_2 and Q_4 are still on, and i_{Lmg} still increases. No currents flow on the secondary side.

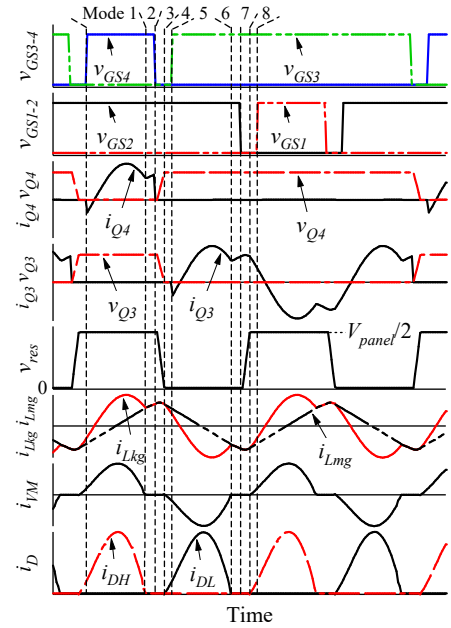*Mode 3* [Fig. 9(c)]: v_{GS4} is removed, and C_{oss3} and C_{oss4} start

Fig. 8. Theoretical operation waveforms.

(a)

(b)

(c)

(d)
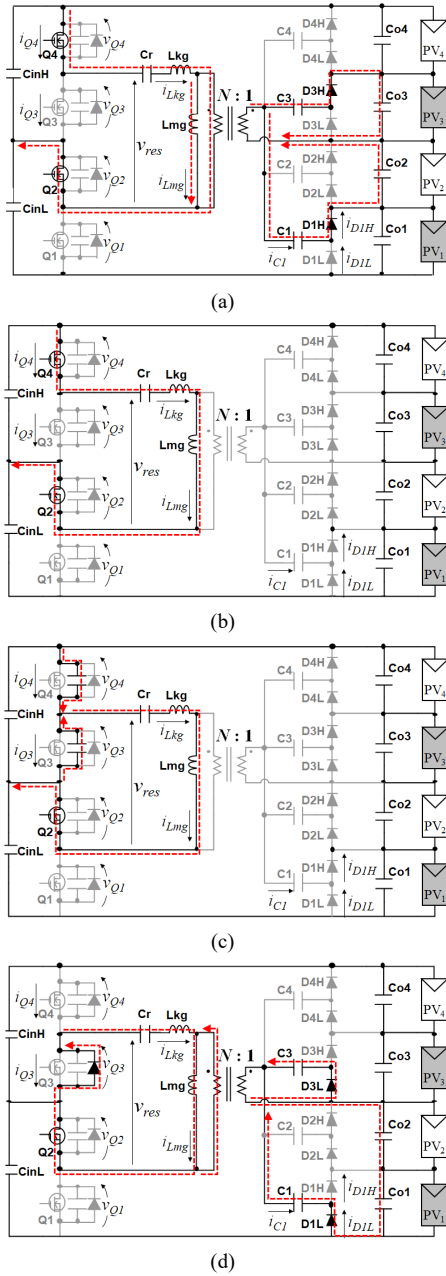
Fig. 9. Current flow path in Mode (a) 1, (b) 2, (c) 3, and (d) 4 when PV_1 and PV_3 are weaker than others.

Fig. 10. DC equivalent circuit.

being discharged and charged by i_{Lmg}, respectively. The voltage of Q_4, v_{Q4}, gradually increases with a slope, achieving ZVS turn-off. At the same time, v_{res} gradually declines as C_{oss3} is discharged. This operation mode ends when v_{Q3} and v_{Q4} reach zero and $V_{panel}/2$, respectively.

Mode 4 [Fig. 9(d)]: As v_{Q3} becomes zero, the body diode of Q_3, D_{b3}, begins to conduct. v_{res} is also zero in this mode as the LLC resonant tank is short-circuited through Q_2 and D_{b3}.

Modes 5–8: While D_{b3} is conducting, v_{GS3} is applied to turn on Q_3 at ZVS. Operations in Mode 5–8 are symmetric to Modes 1–4, and Q_1 and Q_2 are also turned on and off at ZVS.
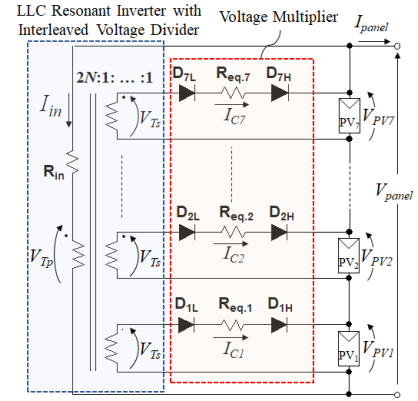
In summary, the voltage applied to the LLC resonant tank,

v_{res}, swings between zero and $V_{panel}/2$ at a frequency twice the switching frequency. On the transformer secondary side, currents flow through diodes that are connected in parallel with weak substrings, whereas other diodes do not conduct. Since average currents of capacitors C_1–C_4 in the voltage multiplier must be zero under steady-state conditions, average diode currents are equal to the currents supplied to weak substrings from the DPP converter.

B. DC Equivalent Circuit

Irradiance levels on the surface of solar roofs significantly vary depending on seasons and time, and hence a simplified model of the DPP converter is indispensable to reduce the simulation burden and time.

A dc equivalent circuit of the conventional DPP converter based on the LLC resonant voltage multiplier was derived in the previous study [30]. The dc equivalent circuit does not contain any switching devices operating at a high frequency, hence allowing efficient and rapid simulation analysis. The proposed DPP converter, shown in Fig. 7, can also be expressed using the same dc equivalent circuit as it is also based on the LLC resonant voltage multiplier.

The dc equivalent circuit of the proposed DPP converter is shown in Fig. 10. The LLC resonant inverter with the interleaved voltage divider is expressed using the combination of an ideal multi-winding transformer and an equivalent input resistance R_{in}. The voltage multiplier is transformed into equivalent resistances $R_{eq.i}$ ($i = 1…7$) sandwiched by diodes. This dc equivalent circuit provides an intuitive understanding of how the DPP converter feeds currents for weak substrings. All the substrings are virtually connected in parallel through the ideal multi-winding transformer, two diodes, and an equivalent resistor $R_{eq.i}$. Hence, a current from the primary winding automatically flows toward weak substrings having lower voltages.

This dc equivalent circuit is essentially identical to that of the conventional DPP converter, except for the turn ratio of the ideal multi-winding transformer. The voltage applied to the LLC resonant tank, v_{res}, is halved by the interleaved voltage divider, and hence, the turn ratio is modified to be $2N{:}1…{:}1$. R_{in} and $R_{eq.i}$ are equivalent resistances that are given by

$$\begin{cases} R_{in} = \dfrac{\pi^2}{2}\left(2r_{DS} + r_{Cr} + r_{Tp} + N^2 r_{Ts}\right) \\[2mm] R_{eq.i} = \dfrac{\omega_r}{\omega_s}\dfrac{\pi^2}{2}\sqrt{r_i^2 + \left(\dfrac{1}{\omega_r C_i}\right)^2} \end{cases} \quad (1)$$

where r_{DS} is the on-resistance of switches, r_{Cr} is the resistance of C$_r$, and r_{Tp} and r_{Ts} are the primary and secondary winding resistances, respectively. ω_s and ω_r ($= 1/\sqrt{L_{kg}C_r}$) are the angular switching frequency and resonant frequency, respectively, r_i and C_i are the resistance and capacitance of C$_i$.

According to the dc equivalent circuit, the following set of equations can be obtained

$$\begin{cases} V_{Tp} = V_{panel} - I_{in}R_{in} \\ V_{Ts} = V_{PVi} + 2V_f + I_{Ci}R_{eq.i} \end{cases} \quad (2)$$

where V_{Tp} and V_{Ts} are the voltage across the primary and secondary windings of the ideal multi-winding transformer, and V_f is the forward voltage drop of diodes. Applying $V_{Tp} = 2NV_{Ts}$ into (2) produces

$$V_{panel} - I_{in}R_{in} = 2N\left(V_{pv.i} + 2V_f + I_{Ci}R_{eq.i}\right) \quad (3)$$

When voltages are uniform under even irradiance conditions, the DPP converter should process no power. In other words, currents in the DPP converter (i.e., I_{in} and I_{Ci} in Fig. 10) should be zero, hence yielding the following operation condition

$$N \geq \frac{V_{panel}}{2\left(V_{PVi} + 2V_f\right)} \quad (4)$$

VI. SIMULATION ANALYSIS

To verify the operation analysis as well as the dc equivalent circuit model derived in Section V, panel characteristics with/without the improved DPP converter in the original circuit (Fig. 7) and the dc equivalent circuit (Fig. 10) were compared in the simulation analysis. Individual substring characteristics modeled in Section II (see Fig. 4) were used for the simulation analysis.

Panel characteristics with/without the DPP converter were swept by varying V_{panel} between zero and an open-circuit voltage. The switching frequency f_s was 100 kHz. The component values of the prototype, which will be shown in Table VII, were applied to the simulation analyses. According to (1) with the component values in Table VII, the equivalent resistance values of R_{in} and $R_{eq.i}$ were determined to be 2.58 Ω and 0.98 Ω, respectively.

Panel characteristics with/without the DPP converter at 9:00 in the original and dc equivalent circuits are compared in Fig. 11(a). The original and dc equivalent circuits showed very similar characteristics. Although unclear, local MPPs were observed in the case without the DPP converter, and the maximum power was 40.4 W. With the DPP converter, the local MPPs vanished, and the maximum power increased to around 43.3 W in both the original and dc equivalent circuit.

Simulation results of the original and dc equivalent circuits at 15:00 are shown in Fig. 11(b). Since the substring characteristics were significantly mismatched in the case at
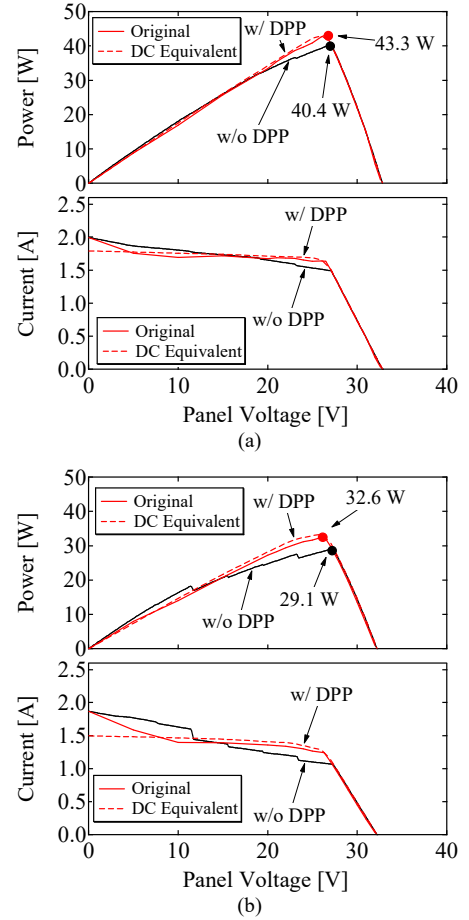

Fig. 11. Panel characteristics with/without DPP converter at (a) 9:00 and (b) 15:00.

15:00, several local MPPs appeared on the *P–V* characteristics of the panel when without the DPP converter. With the DPP converter, on the other hand, the local MPPs disappeared, and the maximum power increased from 29.1 W to 32.6 W.

VII. EXPERIMENTAL RESULTS

A. Prototype

Previous works reported that, based on the statistical case study, DPP converters with power rating equal to 20%–30% of substring power are sufficient to improve annual energy yield
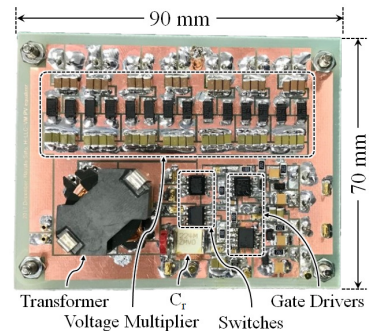

Fig. 12. Photograph of prototype.

TABLE VII
COMPONENT LIST

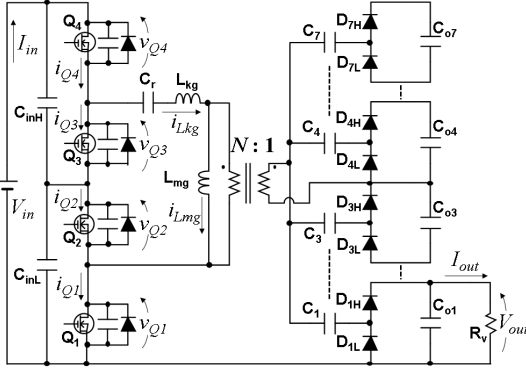| Component	Value
C_{inL}, C_{inH}	Ceramic Capacitor, 22 µF
Q_1–Q_4	Dual MOSFET, IRF7341, r_{DS} = 50 mΩ
C_r	Film Capacitor, 220 nF
Transformer	N_1:N_2 = 9:3, L_{kg} = 1.9 µH, L_{mg} = 199 µH r_{TP} = 286 mΩ, r_{TS} = 10 mΩ
C_1–C_7	Ceramic Capacitor, 88 µF
C_{o1}–C_{o7}	Ceramic Capacitor, 300 µF
D_{1L}–D_{7L}, D_{1H}–D_{7H}	Schottky Barrier Diode, RSX501L V_f = 0.39 V, r_D = 17 mΩ
Gate Driver	UCC27201

Fig. 13. Experimental setup to measure characteristics of DPP converter.

[35], [36]. In this study, a prototype capable of providing 5.0 W for each substring was built for Prius PHEV solar roofs, as shown in Fig. 12. Components used for the prototype are listed in Table VII. The resonant frequency f_r was 256 kHz. The prototype was operated at a fixed f_s of 100 kHz without feedback control.

B. Efficiency and Output Characteristics of DPP Converter

The power conversion efficiency and output characteristics of the DPP converter alone were measured using the experimental setup shown in Fig. 13. The interleaved voltage divider and voltage multiplier were separated by breaking the point X (see Fig. 7). The interleaved voltage divider was powered by an external power supply of V_{in} = 36 V, which was equivalent to the typical MPP voltage of the solar roof. All substrings were removed, and an electronic load R_v operating in a constant resistance mode was connected in parallel with C_{o1} to emulate current flow paths under a case that PV_1 only was weaker than others. The output voltage V_{out} and current I_{out} were measured to calculate the power conversion efficiency η, which is defined as

$$\eta = \frac{V_{out}I_{out}}{V_{ext}I_{ext}} \tag{5}$$

where I_{in} is the input current.

Measured waveforms at I_{out} = 1.0 A are shown in Fig. 14. All switch voltages, as well as the input voltage of the resonant tank v_{res}, changed with slopes, and measured waveforms agreed very well with the theoretical ones.

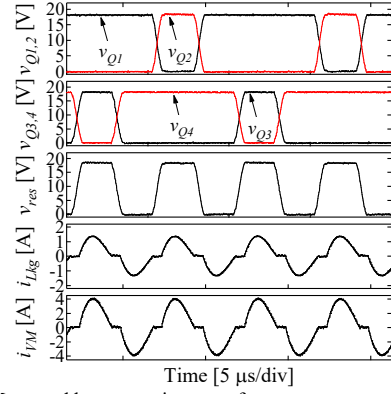The measured power conversion efficiency and output
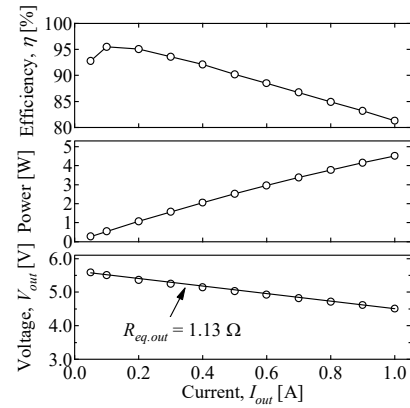

Fig. 14. Measured key operation waveforms.

Fig. 15. Measured output characteristics.

characteristics are shown in Fig. 15. V_{out} (i.e., the voltage of C_{o1}) linearly declined as I_{out} increased. From the measured slope of the characteristic, the equivalent output resistance $R_{eq.out}$ was determined to be 1.13 Ω. Since $R_{eq.out}$ is an equivalent resistance viewed from an output port (or a substring), the theoretical $R_{eq.out}$ can be expressed using R_{in} = 2.58 Ω and $R_{eq.i}$ = 0.98 Ω (see Section VI), as

$$R_{eq.out} = \frac{R_{in}}{N^2} + R_{eq.i} = \frac{2.58\ \Omega}{3^2} + 0.98\ \Omega = 1.26\ \Omega \tag{6}$$

The theoretical $R_{eq.out}$ value of 1.26 Ω satisfactorily agreed with the experimentally determined value of 1.13 Ω.

The efficiency η decreased almost linearly as V_{out} declined or I_{out} increased. This tendency reflected that the portion of V_{out} taken by forward voltage drops of D_{1L} and D_{1H} became significant as V_{out} declined. The measured efficiency at I_{out} = 1.0 A was as high as 81.3%.

C. Laboratory Testing Using Solar Array Simulators

Characteristic mismatches due to the curvature of solar roofs were emulated using solar array simulators (Keysight Technologies, E4361A). Mismatch conditions identical to those in the simulation analysis were used for the experimental verifications. Panel characteristics with/without the DPP converter were swept from short-circuit to open-circuit conditions. An electronic load operating in a constant resistance mode was connected to the panel to sweep the panel
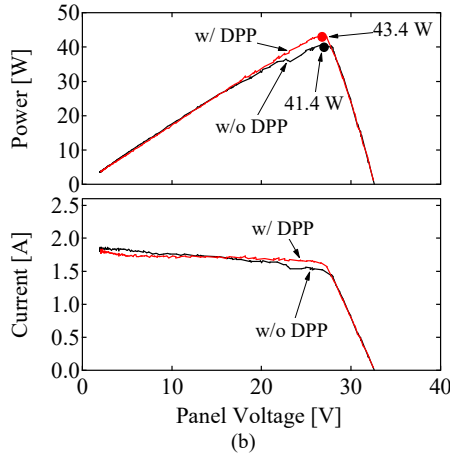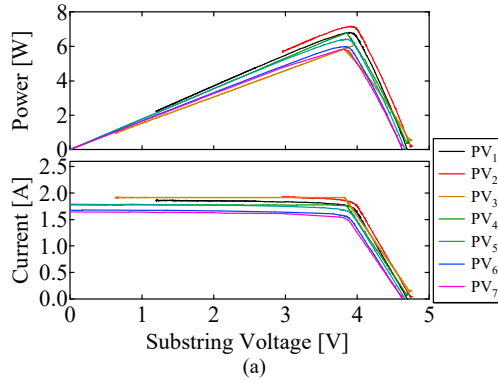
Fig. 16. Experimental results: (a) Individual substring characteristics, (b) panel characteristics with/without DPP converter at 9:00.
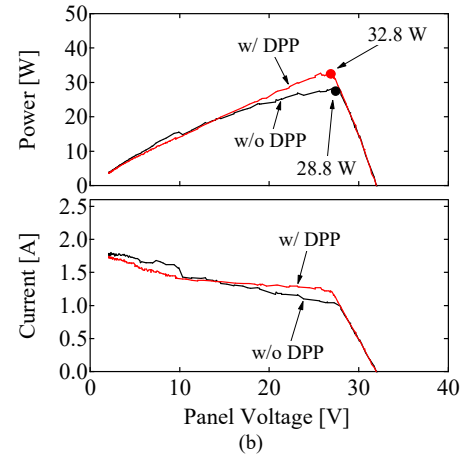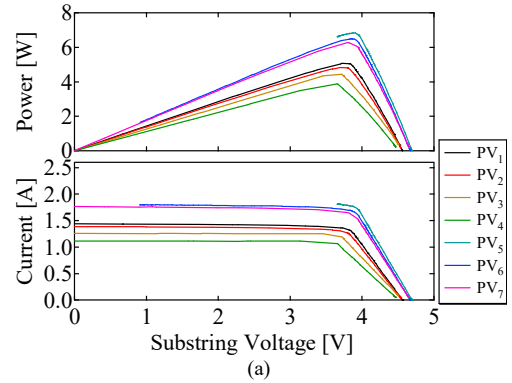

Fig. 17. Experimental results: (a) Individual substring characteristics, (b) panel characteristics with/without DPP converter at 15:00.

characteristics.

Individual substring characteristics emulating the case of 9:00 are shown in Fig. 16(a). The measured panel characteristics with/without the DPP converter are compared in Fig. 16(b). Some local MPPs were observed when without the DPP converter (i.e., with traditional bypass diodes), and the maximum power at the global MPP was 41.4 W. With the DPP converter, on the other hand, the local MPP vanished, and the maximum power increased to as high as 43.4 W, corresponding to 4.8% improvement in power yield.

Substring characteristics and panel characteristics at 15:00 are shown in Figs. 17(a) and (b), respectively. Mismatch in substring characteristics was severer under this condition, and there were several local MPPs observed in the panel's *P–V* characteristic in the case without the DPP converter. In the case with the DPP converter, local MPPs disappeared, and the maximum power improved to as high as 32.8 W from 28.8 W, achieving the significant power yield enhancement of 13.9%.

The experimental panel characteristics in both conditions of 9:00 and 15:00 agreed satisfactorily with those of the dc equivalent circuit (see Fig. 11), verifying the derived dc equivalent circuit.

D. Field Testing

The field testing using an actual solar roof of a Prius PHEV facing east in an open-air parking lot was performed in Miyoshi

City, Japan (east longitude of 137º and northern latitude of 35º), on October 2nd (autumn) and December 25th (winter), 2018. The field test setup is shown in Fig. 18. The DPP converter was placed beneath the solar roof. Panel characteristics with/without the DPP converter was measured for every few minutes on October 2nd and for every minute on December 25th. The irradiance level was measured using a pyranometer (SPM-SD, SATOTECH).

Measured profiles of the panel power P_{panel} and solar irradiance are shown in Fig. 19. On October 2nd [see Fig. 19(a)], profiles of P_{panel} until 10:30 were nearly independent on whether the DPP was enabled, suggesting that the degree of characteristic mismatch was insignificant. Irradiance and P_{panel} fluctuated between 10:30 and 13:40 due to the cloud. After 13:40, the substring characteristic mismatch became significant due to the relationship between the sun angle (θ_E and θ_A) and
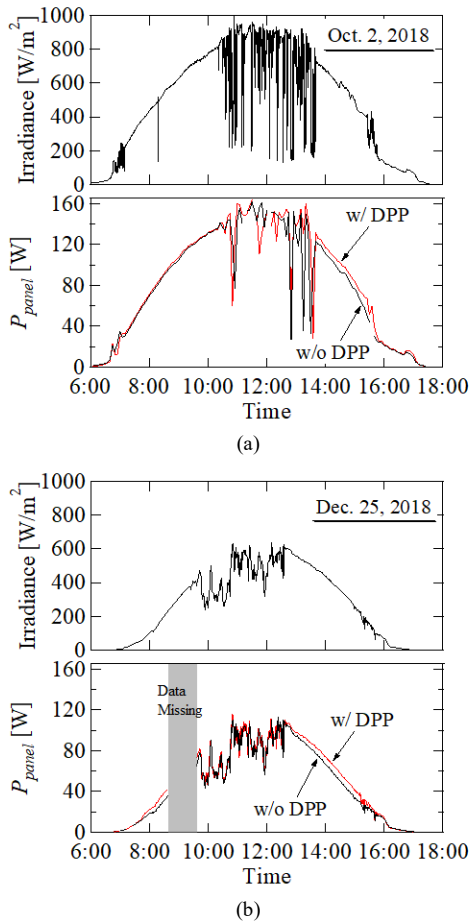

Fig. 18. Field testing setup.

Fig. 19. Power yield and solar irradiance profiles in field testing performed on (a) October 2, 2018 and (b) December 25, 2018.

curvature of the solar roof, and P_{panel} was enhanced by the DPP converter. The approximated daily energy yield was enhanced from 920.8 Wh to 959.1 Wh by the DPP converter, corresponding to 4.2% improvement.

Similar tendencies were observed on December 25th [Fig. 19(b)], but P_{panel} increased clearly not only in the afternoon but also in the morning. This was because substring characteristics were prone to mismatch due to shallow θ_E on December 25th in winter. The energy yields with/without the DPP converter were calculated by integrating P_{panel} over time, except for the data missing period designated in Fig. 19(b). The DPP converter enhanced the daily energy yield from 464.2 Wh to 488.1 Wh, corresponding to 5.2% improvement.

VIII. CONCLUSIONS

Similar to PV panels under partial shading conditions, substring characteristics of solar roofs of PHEVs are unavoidably mismatched due to its curved surface, resulting in the reduced energy yield and the occurrence of multiple MPPs. In this paper, the irradiance mismatch due to the curved surface of solar roofs of Prius PHEV was investigated in order to model mismatched substring characteristics. The investigation results revealed that the degree of mismatch in substring characteristics

varied significantly depending on sun angles because the longitudinal curvature of the solar roof was asymmetric.

Conventional DPP converters and architectures were reviewed to select a proper architecture and topology for PHEV applications. The LLC resonant voltage multiplier was selected as a suitable DPP converter topology and was improved to be better suitable for PHEV applications.

The operation analysis was performed for the improved LLC resonant voltage multiplier, followed by the derivation of the dc equivalent circuit. Characteristics of the solar roof without the DPP converter (i.e., with traditional bypass diodes) in simulation analyses exhibited multiple MPPs. With the DPP converter, on the other hand, the local MPPs vanished, and maximum powers increased. The results of the original and dc equivalent circuits agreed well, verifying the derived equivalent circuit model.

The DPP converter prototype was built and tested in the laboratory. The field testing using the actual solar roof of Prius PHEV in an open-air parking lot was also performed with/without the DPP converter prototype. The results of the field testing demonstrated that the DPP converter enhanced daily energy yield by 4%–5%.

REFERENCES

[1] S.M. MacAlpine, R.W. Erickson, and M.J. Brandemuehl, "Characterization of power optimizer potential to increase energy capture in photovoltaic systems operating under nonuiform conditions," *IEEE Trans. Power Electron.*, vol. 28, no. 6, pp. 2936–2945, Jun. 2013.

[2] H. Jeong, H. Lee, Y.C. Liu, and K.A. Kim, "Review of differential power processing converters techniques for photovoltaic applications," *IEEE Trans. Energy Conversion*, vol. 34, no. 1, pp. 351–360, Mar. 2019.

[3] H.J. Bergveld, D. Büthker, C. Castello, T. Doorn, A.D. Jong, R.V. Otten, and K.D. Waal, "Module-level dc/dc conversion for photovoltaic systems: the delta-conversion concept," *IEEE Trans. Power Electron.*, vol. 28, no. 4, pp. 2005–2013, Apr. 2013.

[4] M.S. Zaman, Y. Wen, R. Fernandes, B. buter, T. Doorn, M. Dijkstra, H.J. Bergveld, and O. Trescases, "A cell-level differential power processing IC for concentrating-PV systems with bidirectional hysteretic current-mode control and closed-loop frequency regulation," *IEEE Trans. Power Electron.*, vol. 30, no. 12, pp. 7230–7244, Dec. 2015.

[5] P.S. Shenoy, K.A. Kim, B.B. Johnson, and P.T. Krein, "Differential power processing for increased energy production and reliability of photovoltaic systems," *IEEE Trans. Ind. Power Electron.*, vol. 28, no. 6, pp. 2968–2979, Jun. 2013.

[6] S. Qin, S.T. Cady, A.D.D. García, and R.C.N. Podgurski, "A distributed approach to maximum power point tracking for photovoltaic submodule differential power processing," *IEEE Trans. Power Electron.*, vol. 30, no. 4, pp. 2024–2040, Apr. 2015.

[7] S. Qin, C.B. Barth, and R.C.N. Podgurski, "Enhancing microinverter energy capture with submodule differential power processing," *IEEE Trans. Power Electron.*, vol. 31, no. 5, pp. 3575–3585, May 2016.

[8] F. Wang, T. Zhu, F. Zhuo, and H. Yi, "An improved submodule differential power processing-based PV system with flexible multi-MPPT control," *IEEE J. Emerging Selected Topics*, vol. 6, no. 1, pp. 94–102, Mar. 2018.

[9] T. Shimizu, O, Hashimoto, and G. Kimura, "A novel high-performance utility-interactive photovoltaic inverter system," *IEEE Trans. Power Electron.*, vol. 18, no. 2, pp. 704–711, Mar. 2003.

[10] T. Shimizu, M. Hirakata, T. Kamezawa, and H. Watanabe, "Generation control circuit for photovoltaic modules," *IEEE Trans. Power Electron.*, vol. 16, no. 3, pp. 293–300, May 2001.

[11] M.Z. Ramli and Z. Salam, "A simple energy recovery scheme to harvest the energy from shaded photovoltaic modules during partial shading," *IEEE Tran. Power Electron.*, vol. 29, no. 12, pp. 6458–6471, Dec. 2014.

[12] J.T. Stauth, M.D. Seeman, and K. Kesarwani, "Resonant switched-capacitor converters for sub-module distributed photovoltaic power management," *IEEE Trans. Power Electron.*, vol. 28, no. 3, pp. 1189–1198, Mar. 2013.

[13] A.H. Chang, A.T. Avestruz, and S.B. Leeb, "Capacitor-less photovoltaic cell-level power balancing using diffusion charge redistribution," *IEEE Trans. Power Electron.*, vol. 30, no. 2, pp. 537–546, Feb. 2015.

[14] A. Blumenfeld, A. Cervera, and M.M. Peretz, "Enhanced differential power processor for PV systems: resonant switched-capacitor gyrator converter with local MPPT," *IEEE J. Emerging Selected Topics in Power Electron.*, vol. 2, no. 4, pp. 883–892, Dec. 2014.

[15] Z. Qiu and K. Sun, "A photovoltaic generation system based on wide voltage-gain DC-DC converter and differential power processors for DC microgrids," *Chinese J. Electrical Engineering*, vol. 3, no. 1, pp. 84–95, Jun. 2017.

[16] M. Gokdaga, M. Akbabab, and O. Gulbudakc, "Switched-capacitor converter for PV modules under partial shading and mismatch conditions," *Solar Energy*, vol. 170, pp. 723–731, Aug. 2018.

[17] M. Uno and A. Kukita, "PWM converter integrating switched capacitor converter and series-resonant voltage multiplier as equalizers for photovoltaic modules and series-connected energy storage cells for exploration rovers," *IEEE Trans. Power Electron.*, vol. 32, no. 11, pp. 8500–8513, Nov. 2017.

[18] M. Uno, Y. Saito, M. Yamamoto, and S. Urabe, "PWM switched capacitor-based cell-level power balancing converter utilizing diffusion capacitance of photovoltaic cells," *IEEE Trans. Power Electron.*, to be published.

[19] M. Uno, M. Yamamoto, H. Sato, and S. Oyama, "Modularized differential power processing architecture based on switched capacitor converter to virtually unify mismatched photovoltaic panel characteristics," *IEEE Trans. Power Electron.*, to be published.

[20] C. Olalla, D. Clement, M. Rodríguez, and D. Makisimović, "Architectures and control of submodule integrated dc-dc converters for photovoltaic applications," *IEEE Trans. Power Electron.*, vol. 28, no. 6, pp. 2980–2997, Jun. 2013.

[21] Y. Levron, D.R. Clement, B. Choi, C. Olalla, and D. Maksimovic, "Control of submodule integrated converters in the isolated-port differential power-processing photovoltaic architecture," *IEEE J. Emerging Selected Topics in Power Electron.*, vol. 2, no. 4, pp. 821–832, Dec. 2014.

[22] R. Bell and R.C.N.P. Podgurski, "Decoupled and distributed maximum power point tracking of series-connected photovoltaic submodules using differential power processing," *IEEE J. Emerging Selected Topics in Power Electron.*, vol. 3, no. 4, pp. 881–891, Dec. 2015.

[23] C. Olalla, C. Deline, D. Clement, Y. Levron, M. Rodríguez, and D. Makisimović, "Performance of power limited differential power processing architectures in mismatched PV systems," *IEEE Trans. Power Electron.*, vol. 30, no. 2, pp. 618–631, Feb. 2015.

[24] G. Chu, H. Wen, L. Jiang, Y. Hu, and X. Li, "Bidirectional flyback based isolated-port submodule differential power processing optimizer for photovoltaic applications," *Solar Energy*, vol. 158, pp. 929–940, Oct. 2017.

[25] Y.T. Jeon, H. Lee, K.A. Kim, and J.H. Park, "Least power point tracking method for photovoltaic differential power processing systems," *IEEE Trans. Power Electron.*, vol. 32, no. 3, pp. 1941–1951, Mar. 2017.

[26] Y.T. Jeon and J.H. Park, "Unit-minimum least power point tracking for the optimization of photovoltaic differential power processing systems," *IEEE Trans. Power Electron.*, vol. 34, no. 1, pp. 311–324, Jan. 2019.

[27] J. Du, R. Xu, X. Chen, Y. Li, and J. Wu, "A novel solar panel optimizer with self-compensation for partial shadow condition," in Proc. *IEEE Applied Power Electron. Conf. Expo., APEC*, pp. 92–96, 2013.

[28] M. Uno and A. Kukita, "Single-switch voltage equalizer using multi-stacked buck-boost converters for partially-shaded photovoltaic modules," *IEEE Trans. Power Electron.*, vol. 30, no. 6, pp. 3091–3105, Jun. 2015.

[29] M. Uno and A. Kukita, "Current sensorless equalization strategy for a single-switch voltage equalizer using multistacked buck–boost converters for photovoltaic modules under partial shading," *IEEE Trans. Ind. Appl.*, vol. 53, no. 1, pp. 420–429, Jan./Feb. 2017.

[30] M. Uno and A. Kukita, "Two-switch voltage equalizer using an LLC resonant inverter and voltage multiplier for partially-shaded series-connected photovoltaic modules," *IEEE Trans. Ind. Appl.*, vol. 51, no. 2, pp. 1587–1601, Mar./Apr. 2015.

[31] M. Uno and A. Kukita, "Single-switch single-magnetic PWM converter integrating voltage equalizer for partially-shaded photovoltaic modules in standalone applications," *IEEE Trans. Power Electron.*, vol. 33, no. 2, pp. 1259–1270, Feb. 2018.

[32] M. Uno and T. Shinohara, "Module-integrated converter based on cascaded quasi-Z-source inverter with differential power processing capability for photovoltaic panels under partial shading," *IEEE Trans. Power Electron.*, to be published.

[33] J. Cao, N. Schofield, and A. Emadi, "Battery balancing methods: A comprehensive review," in Proc. *IEEE Veh. Power Propulsion Conf.*, Sep. 2008, pp. 1–6.

[34] C.W.T. McLyman, Transformer and inductor design handbook, New York: CRC Press, 2011, ch.5.4.

[35] K.A. Kim, P.S. Shenoy, and P.T. Krein, "Converter rating analysis for photovoltaic differential power processing systems," *IEEE Trans. Ind. Electron.*, vol. 30, no. 4, pp. 1987–1997, Apr. 2015.

[36] C. Olalla, M.N. Hasan, C. Deline, and D. Maksimovi, "Mitigation of hot-spots in photovoltaic systems using distributed power electronics," *Energies*, vol. 11, Mar. 2018.

Masatoshi Uno (M'06) was born in Japan in 1979. He received the B.E. degree in electronics engineering and the M.E. degree in electrical engineering from Doshisha University, Kyoto, Japan, and the Ph.D. degree in space and astronautical science from the Graduate University for Advanced Studies, Hayama, Japan, in 2002, 2004, and 2012, respectively.

In 2004, he joined the Japan Aerospace Exploration Agency, Sagamihara, Japan, where he developed spacecraft power systems including battery, photovoltaic, and fuel cell systems. In 2014, he joined the Department of Electrical and Electronics Engineering, Ibaraki University, Ibaraki, Japan, where he is currently an Associate Professor of Electrical Engineering.

His research interests include switching power converters for renewable energy systems, life evaluation for EDLCs and lithium-ion batteries, and development of spacecraft power systems. Dr. Uno received the Isao Takahashi Power Electronics Award in 2018.

Hayato Sato was born in Japan in 1996. He received the B.E. degree and M.E degree in electrical engineering from Ibaraki University, Ibaraki, Japan, in 2018 and 2020, respectively. He is currently with Hitachi Ltd. His research interests include switching converters for photovoltaic systems.

Tetsuaki Ishikawa was born in Japan in 1991. He received the B.E. degree in Faculty of Engineering from Toyota Technological Institute, Aichi, Japan, in 2010 and 2015, respectively. He is currently with Kojima Industries Corporation. His research interests include switching converters for photovoltaic systems.